Determination of the Ice Particle Size Distributions Using Observations as the Integrated Constraints

Jun-Ichi Yano, Andrew J Heymsfield, Aaron Bansemer

To cite this version:

Jun-Ichi Yano, Andrew J Heymsfield, Aaron Bansemer. Determination of the Ice Particle Size Distributions Using Observations as the Integrated Constraints. Journal of the Atmospheric Sciences, 2018, ⟨10.1175/JAS-D-17-0145.1⟩. ⟨hal-02395958⟩

HAL Id: hal-02395958

https://hal.science/hal-02395958v1

Submitted on 5 Dec 2019

Determination of the Ice Particle Size Distributions Using Observations as the Integrated Constraints

JUN-ICHI YANO

CNRM UMR 3589, Météo-France/CNRS, Toulouse, France

ANDREW J. HEYMSFIELD AND AARON BANSEMER

NCAR, Boulder, Colorado

(Manuscript received 5 May 2017, in final form 18 September 2017)

ABSTRACT

The possibility is suggested of estimating particle size distributions (PSD) solely based on the bulk quantities of the hydrometeors. The method, inspired by the maximum entropy principle, can be applied to any predefined general PSD form as long as the number of the free parameters is equal to or less than that of the bulk quantities available. As long as an adopted distribution is ''physically based,'' these bulk characterizations can recover a fairly accurate PSD estimate.

This method is tested for ice particle measurements from the Tropical Composition, Cloud and Climate Coupling Experiment (TC4). The total particle number, total mass, and mean size are taken as bulk quantities. The gamma distribution and two distributions obtained under the maximum entropy principle by taking the size and the particle mass, respectively, as a restriction variable are adopted for fit. The fitting error for the two maximum entropy–based distributions is comparable to that of a standard direct fitting method with the gamma distribution. The same procedure works almost equally well when the mean size is removed from the constraint, especially for an exponential distribution.

The results suggest that the total particle number and the total mass of the hydrometeors are sufficient for determining the PSD to a reasonable accuracy when a ''physically based'' distribution is assumed. In addition to the in situ cloud measurements, remote sensing measurements such as those from radar as well as satellite can be adopted as physical constraints. Possibilities of exploiting different types of measurements should be further pursued.

1. Introduction

It is a common practice to fit observed hydrometeor particle size distributions (PSDs) into a known distribution form. A typical choice is the gamma distribution (Ulbrich 1983; Willis 1984). One may even hope that by fitting an observed PSD into a known function form, the PSD may be extrapolated beyond the observed range, if the chosen function form is physically based in a robust manner. If such a procedure is possible, the various characteristics for PSDs such as the total particle number and the mean particle mass would also be better estimated as a result. Such a possibility has led to consideration for a new methodology for determining the hydrometeor PSDs, inspired from the maximum entropy principle.

The maximum entropy principle defines the statistically most likely distribution of a variable under a given set of physical integral constraints (Jaynes 2003). This procedure consists of the two major steps. First, a general form of the distribution is derived under a given set of constraints. Second, free parameters of the distribution are determined from the given physical values for these constraints.

A basic starting point of the present study is to note that the above second step can be taken out from the whole procedure and be used in a standalone manner. Here, in general, the system may not follow the most likely distribution as defined from the maximum entropy principle. However, whatever way it may be defined, if

---

Denotes content that is immediately available upon publication as open access.

Corresponding author: Jun-Ichi Yano, jiy.gfder@gmail.com

DOI: 10.1175/JAS-D-17-0145.1

an assumed general form of the distribution is physically based, to that extent, a finite set of physical integral constraints would accurately determine the distribution even without referring to an observed distribution directly. The present paper applies this idea to the ice hydrometeor PSDs by taking these integral physical constraints to be the total particle concentration N_T, the mean particle mass $\overline{m}$ (or total particle mass $\overline{M}$), and the number concentration–weighted mean size $\overline{D}$.

If such a procedure is possible in general, there would no longer be a need for measuring the PSD except for the total particle concentration. Instead, we just need to focus on the less difficult measurements of the bulk quantities of the hydrometeors such as the total mass per volume. The present paper explores this possibility.

The paper is organized as follows. The hydrometeor data to be analyzed in the study is described in the next section. Some basic characteristics of the hydrometeor measurements are also discussed therein. Some of the measurement uncertainties described therein provide the further motivations for a new PSD fitting method. The traditional methodology for determining the PSD is reviewed in section 3, and a new methodology is introduced in section 4. PSDs are analyzed in section 5 based on both traditional and new methods, and the results are compared. The paper concludes with a summary and further discussion in section 6.

2. Data

a. Study case

Data from the Tropical Composition, Cloud and Climate Coupling Experiment (TC4; Toon et al. 2010) are taken for the study. TC4 was conducted over Costa Rica and the Caribbean during July and August 2007 with a focus on convective clouds. A flight leg on 8 August for ice particle measurements is used for the present study. This particular leg was chosen since it was the longest continuous in-cloud leg during the project with cold temperatures in a relatively dense anvil cloud. The analysis is limited to the period of 1230–1530 UTC in order to ensure that only the full ice phase is considered in the temperature range from −35° to −50°C. The data are averaged over 5-s intervals corresponding approximately to a 1-km flight segment (Fig. 1).

b. Instruments and measurements

For measuring properties of the ice particles, the cloud imaging probe (CIP) is used for the range of 25 μm–1 mm, and the precipitation imaging probe (PIP) for the range of 1–30 mm. These particle probes measure the size of each observed particle. Additionally, the counterflow virtual impactor (CVI) measures the total hydrometeor mass per volume [ice water content (IWC)] by vaporizing the ice particles within the zero-humidity air (Ogren et al. 1985; Noone et al. 1988; Twohy et al. 1997).

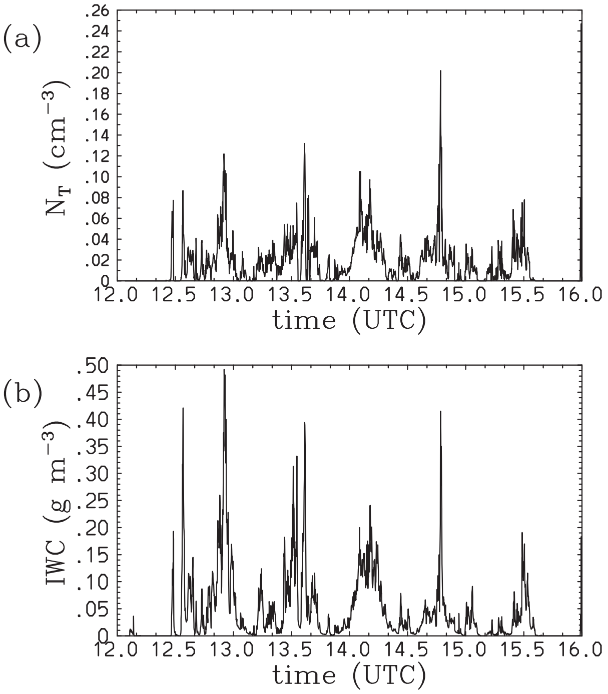

FIG. 1. Time series of (a) the observed total particle number density N_T and (b) the IWC during the flight lag adopted for the present study. Note that the analysis period spans 1230–1530 UTC.

The mass m of an individual ice particle may be estimated from the formula

$$m = aD^b \tag{2.1}$$

(Locatelli and Hobbs 1974; Mitchell et al. 1990; Brown and Francis 1995; Baker and Lawson 2006; Schmitt and Heymsfield 2009), where D is maximum dimension (“size” in short) of the particle. By taking a sum of all those particle mass estimates, we also obtain the IWC. In this manner, the particle probes can provide an estimate of IWC separately from CVI (Heymsfield et al. 2004). Here, the parameters, a and b, in Eq. (2.1) are determined in such a manner that the IWCs obtained from the particle probes are consistent with those from CVI. More precisely, we have determined a and b such that the average mass over the whole analysis period (1230–1530 UTC) from the particle probes agrees with that from CVI, and the standard deviation of the mass estimate by (2.1) from CVI measurements is minimized. As a result, we obtain $a = 2.056 \times 10^{-3}\,\mathrm{g\,cm}^{-b}$ and $b = 1.878$. In preliminary phase of the investigation, various different values for b are used, and we found no strong sensitivity of the result on the choice of this value. Here, in this evaluation, the errors of CVI are not explicitly taken into account.

Arguably, a major function of the particle probes is to count the total number of hydrometeor particles. However, these instruments do not "count" the particles in literal sense. First of all, these two particle probes do not have the same sample volume: the CIP has a quarter of the sample volume of the PIP. Furthermore, the effective sample volume depends on the particle size owing to the optics of the instrument and the way that partially imaged particles are handled, especially those that touch an edge of the image area. Thus, each particle count contributes to the total particle number with a weight inversely proportional to its effective sample volume. In this manner, the uncertainty of the particle size estimate also affects the estimate of the particle concentration. For further basic technical issues of the particle probes, see Heymsfield and Parrish (1978).

The particle size range recorded by the probes is typically from 25 μm to several centimeters in size. However, the probes do not measure all particle sizes with equal accuracy. Measurement uncertainties are higher for smaller particles, and measurements below 100 μm in size are particularly unreliable owing to the effects of shattering (Korolev et al. 2013) and optical limitations. Reported concentrations of smaller particles are often unrealistically large for these reasons. Larger particles are often only partially seen in the image area, and those above a certain size need to be excluded.

With these considerations, all the measurements below 100 μm are excluded from the present analysis. The remaining measurements from both probes are tabulated by dividing these ranges into 34 bins. The first three bins have the size ranges of [100 μm, 150 μm], [150 μm, 200 μm], [200 μm, 250 μm], and the last bin considered is [16 mm, 18 mm]. The bin sizes increases roughly logarithmically with the increasing size. Furthermore, in the analysis of section 6, the three particle size ranges are considered: (i) the full range, 100 μm–18 mm; (ii) the medium range, 150 μm–10 mm, which excludes least-reliable measurements; and (iii) the narrow range (550 μm–5 mm), in which only the most reliable measurements are retained. In the small-size limit, depth of field uncertainty is reduced beyond 150 μm and shattering uncertainties are reduced beyond 550 μm, since most shattered particles are smaller than this. In the large-size limit, a 5-mm limit stays within the array width of the PIP (6.4 mm), and 10 mm includes particles where a reasonable size may be estimated from a partial image.

The basic principle of the CVI is to sublimate or vaporize all the condensed water within a zero-relative-humidity environment, and thus the total condensed water content (IWC for the present study) is obtained. However, not all the hydrometeors are captured into the inlet. First, the inlet diameter is 5.8 mm; thus, any particles larger than this size would not fully enter the inlet, and large particles of comparable sizes are not sampled effectively, either. We, rather arbitrarily, assume the maximum size that enters the inlet to be 2 mm in the following analysis. Particles must also have enough inertia to penetrate the counterflow at the probe inlet, preventing very small particles from entering the instrument (Ogren et al. 1985). We assume the minimum size to be 7 μm. By comparison with the particle imaging probes, the IWC values less than 0.01 g m^{-3} were removed from the analysis so that the errors from residual vapor/condensate in the CVI plumbing after exiting cloud are much reduced. Furthermore, CVI measurements saturate above the upper limit of the instrument's capability to fully evaporate the liquid water, at about 2 g m^{-3} (Heymsfield et al. 2009). By limiting the data in this manner, the total of 1427 samples is considered in the present study.

c. *Basic characteristics of the measurements*

A major issue with the particle probes is that the particle count is not very reliable right at the edge of the resolution of the probe (25 μm in the present case). Uncertainties are also introduced into mass estimation owing to ambiguities in estimating the particle size at the resolution limit and with out-of-focus ice particle images. The cutoff at larger sizes makes the data more reliable. However, a deeper cutoff leads to a further "undercounting" of both particle concentration and the total mass (IWC). Here, note that the IWC is defined by an integral over a finite size range [Eq. (4.6) below]. Examining this effect is important for understanding the uncertainties in estimating PSDs.

Figure 2a plots the frequency distribution of the fractional particle number counted when the cutoff sizes are increased from 100 to 150 (solid) and to 200 μm (long dashed). It is most likely that the total particle count decreases by about 30% by increasing the cutoff size to 150 μm. A substantially long tail in the distribution suggests that undercounting could be substantially worse. A further increase to 200 μm clearly loses more counts and the most likely fractional number retained is about 50% with a fairly wide distribution.

Figure 2b shows the ratio of the IWC estimated by the particle probes to that measured by CVI [see also Fig. 3 of Heymsfield et al. (2013)]. Recall that the full particle probe data are tuned to provide an average IWC identical to that from CVI. This fact is confirmed by the maximum frequency corresponding to the ratio of unity

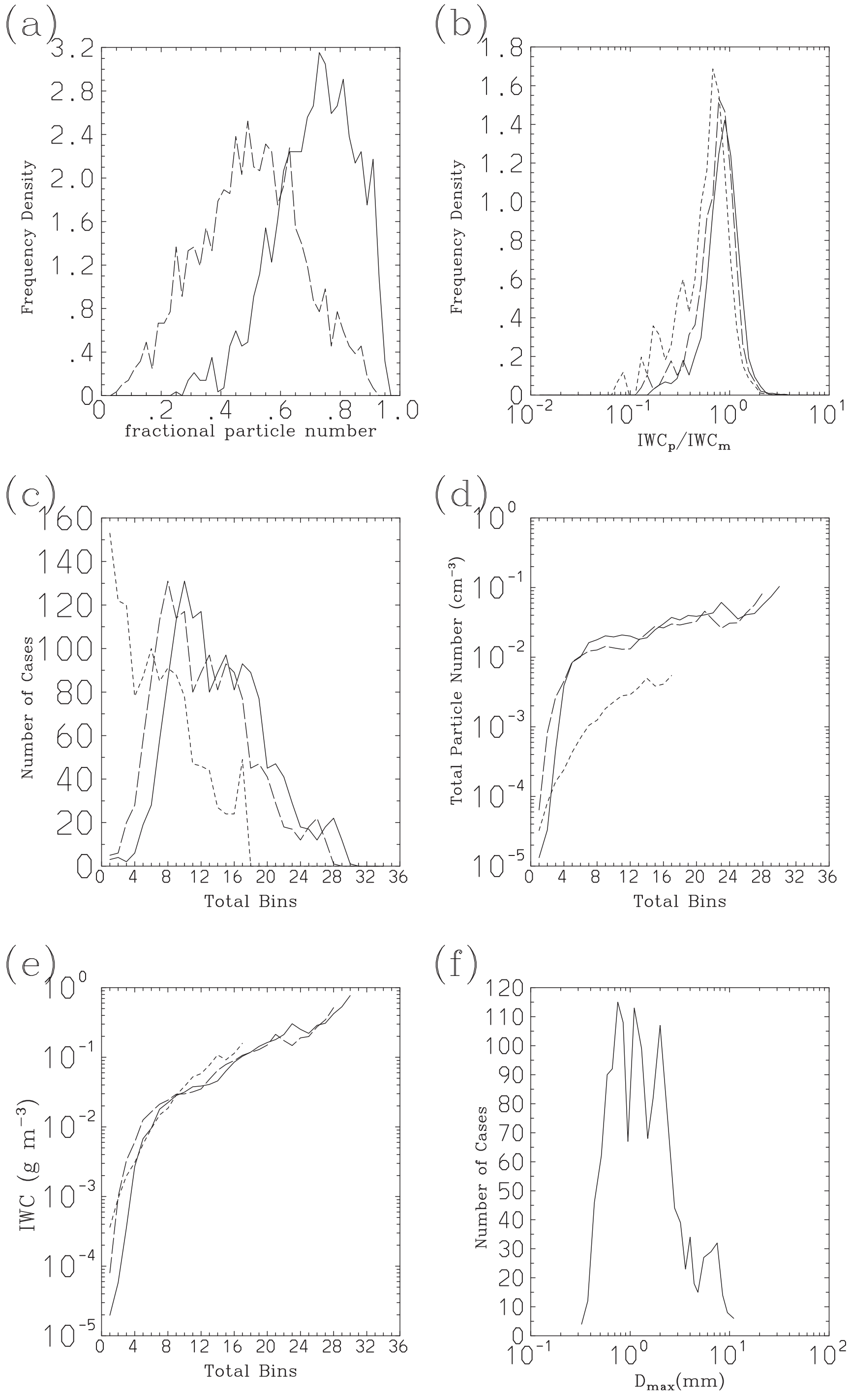

FIG. 2. Various characterizations of the observations during the flight leg adopted for the present study. (a) The frequency distribution of the fractional particle concentration relative to the full data with the cutoff sizes 150 (solid) and 200 μm (long dashed). (b) The frequency distribution of the IWC ratio: IWC_p/IWC_m. Here, IWC_p is IWC based on the particle probe measurements, and IWC_m is IWC based on CVI. The three curves are for IWC_p with the cutoff size: 100 (solid), 150 (long dashed), and 200 μm (short dashed). (c) As in (b), but for the number of cases against the total number of the counted bins. (d) As in (c), but for the mean total particle concentration N_T. (e) As in (c), but for the mean IWC. (f) Number of cases as a function of the maximum size measured.

when the full data are considered (solid curve). A long tail toward the small ratio, $\mathrm{IWC}_p/\mathrm{IWC}_m$, may also be worthwhile to note. This long tail may partially be explained by the tendency of the CVI measurements to smooth out the time series due to the hysteresis, as well as the saturation of the instrument. Here, coincidentally, the three IWC ratio curves corresponding to the three cutoff sizes match the other relatively well, though the curves shift leftward with increasing cutoff sizes (as they should).

To perform a reliable PSD estimate, the available number of particle bins must be large enough. In Fig. 2c, the solid curve shows a number distribution of the counted number of particle bins during the flight leg. The most frequently found bin number is 10, with the range of 8–18 fairly frequent. A few flight segments contain only one particle bin measurement, whereas the maximum number of bins counted is 30. No flight segment counted all the possible particle bins. When the size range is slightly limited to [150 μm, 10mm] (long dashed), the distribution simply shifts to the left by about the two bins. However, when the size range is further limited to [0.55mm, 5mm] (short dashed), the frequency simply decreases with the increasing total bin numbers (with an exception of a minor peak at 17 bins). See Hallett (2003) for discussions on the errors associated with a particle number counting per bin.

To see a possible reason for missing measurements at given bins, the mean for total counted particle number N_T (cm^{-3}) is plotted as a function of the total measured bin numbers for the full (solid), the medium (150 μm–10 mm: long dashed), and the narrow ranges (0.55 μm–5 mm: short dashed) in Fig. 2d. Regardless of the cutoff sizes, the total particle concentration presents a clear trend of increasing with increasing available bin numbers. This leads to the natural interpretation that a low number of counted bins typically occurs when the total particle concentration is also low. Under such a situation, a particle is counted at a certain bin by chance, and not in the others by chance, because the turbulent flow within the cloud stirs the particles intermittently in a random-looking manner (Ottino 1989). As a result, interpolating the counted bin values may even not be a good idea. Note that the number of missing bins can be reduced by taking a longer averaging time for sampling, but at the expense of reduced spatial resolution. Figure 2e shows the same, but for the IWC.

Similar statistics can be taken as functions of the maximum particle size $D_{\max}$ measured. Figure 2f shows that most of the flight segments correspond to the maximum size of the range from 0.2–0.3 to 2–3 mm. Recall that the maximum ice particle available for a measurement is 18 mm. We further find that the available fraction roughly monotonically decreases with the increasing maximum measured size. When the maximum size is larger than 3 mm, the missing fraction may be larger than 10%.

3. Traditional PSD estimate method

Traditionally, the determination of the PSD is considered a curve fitting problem. A common technique used in the literature (Ulbrich 1983; Willis 1984) is to adopt a gamma distribution

$$N(D) = N_0 D^{\mu} \exp(-\lambda D) \tag{3.1}$$

as a general form of the PSD as a function of the size D. The observed PSD is fitted to this general form by adjusting the three constants: N_0, μ, and λ.

Is it mathematically known (e.g., Durrett 2010) that the moments can completely characterize a distribution in an analogous manner as the Taylor-expansion coefficients for the analytical functions. Thus, a natural choice is to estimate a distribution form by a set of moments:

$$M_{\mathrm{obs}}(q) = \int_{D_{\min}}^{D_{\max}} N_{\mathrm{obs}}(D) D^q \, dD \tag{3.2}$$

from the observed PSD $N_{\mathrm{obs}}(D)$. Here, $D_{\min}$ and $D_{\max}$ are the minimum and the maximum sizes of the particles measured. A standard procedure (e.g., Kozu and Nakamura 1991; Heymsfield et al. 2002; Zhang et al. 2003; Schmitt and Heymsfield 2009) is to choose three moments from the above for estimating the three unknown constants in the gamma distribution.

Here, McFarquhar et al. (2015) emphasize the importance of explicitly considering the finite size range for the measurements as explicitly stated in Eq. (3.2). On the other hand, a common custom is to take the limit of $D_{\min} = 0$ and $D_{\max} \rightarrow +\infty$ so that the moments under the gamma distribution can be evaluated by an analytical formula:

$$M(q) = \frac{N_0}{\lambda^{\mu+p+1}} \Gamma(\mu + q + 1). \tag{3.3}$$

Here, $\Gamma(x)$ is the gamma function. By comparing Eqs. (3.2) and (3.3), we obtain a general constraint on the gamma distribution from the observed distribution given by

$$\frac{N_0}{\lambda^{\mu+q+1}} \Gamma(\mu + q + 1) = M_{\mathrm{obs}}(q). \tag{3.4}$$

Thus, once any three moments are known from the observed PSD, Eq. (3.4) can be used, in principle, for evaluating the three constants of the distribution. The choice of the set of moments remains rather arbitrary.

However, by following Heymsfield et al. (2002), we take $q = 1, 2, 6$. These first two moments anchor the small end of the gamma fit. We also adopt the sixth moment, because it is found to be desirable to use a sufficiently high-order moment in order to anchor the large end of the fit.

See Smith and Kliche (2005), Kliche et al. (2008), Mallet and Barthes (2009), Smith et al. (2009), and Handwerker and Straub (2011) for discussions on the sampling errors associated with the standard estimate method.

4. New PSD estimate method

In the present study, on the other hand, we consider the determination of the PSD more as a physical problem. As pointed out in Yano et al. (2016), any physical system may be constrained by a set of conditions

$$C_l = \int_{D_{\min,l}}^{D_{\max,l}} F_l(N, D)\, dD \qquad (4.1)$$

for $l = 1, \ldots, n$. Here, $F_l(N, D)$ are any functions of the number density distribution $N(D)$, and the particle size, D (or any other physical variables), that define forms of physical constraints. A generality of the form of the function F_l introduced here is hardly overemphasized, which is not restricted to the moments or anything similar (cf. section 6d). The constraint constant C_l is estimated from observation. We may take different integral ranges $[D_{\min,l}, D_{\max,l}]$ for different constraints based on the instrument constraints.

When a general distribution form of the problem

$$N(D) = N(D; \lambda_1, \ldots, \lambda_n), \qquad (4.2)$$

defined in terms of the n parameters λ_l ($l = 1, \ldots, n$) is known, a set of the constraints (4.1) is sufficient for determining a distribution. Note that in order for this methodology to work well, the general distribution form (4.2) must be physically based in a certain sense so that its universality is guaranteed. Here, we do not count the normalization constant n_0 as one of the parameters to be determined, because once all the other parameters are known, this is defined simply from the normalization condition (see appendix).

More specifically, the maximum entropy principle suggests, as explicitly shown in Yano et al. (2016), that under these constraints, the most likely distribution is given by

$$N(D) = n_0 \exp\left(-\sum_{l=1}^{n} \lambda_l \frac{\partial F_l}{\partial N}\right) \qquad (4.3)$$

with the constants λ_l ($l = 1, \ldots, n$) defined by the conditions (4.1). This distribution (4.3) may be considered a particular case of the more general principle just outlined.

A mathematically straightforward procedure to satisfy the n conditions given by Eq. (4.1) is to minimize the quantity

$$\epsilon = \sum_{l=1}^{n} \left[1 - \frac{1}{C_l} \int_{D_{\min,l}}^{D_{\max,l}} F_l(N, D)\, dD\right]^2 \qquad (4.4)$$

against the given parameters λ_l ($l = 1, \ldots, N$) for a given general distribution form (4.2). This is the procedure also adopted herein. The numerical procedure for the minimization is described in the appendix, separately. Note that the particular adopted numerical procedure is merely for the purpose of demonstration. A different numerical scheme may be sought in operational implementations, especially for improving the success rate of the estimation (cf. section 5a).

To some extent, a set of the constraints (4.1) may be considered a generalization of the moment constraints given by Eq. (3.2) in the last section. However, this generalization is associated with two major implications. First, the constraint itself can be generalized in any possible manner. The exponent in the moment may not be necessarily constrained to integers, and a fractional power may be considered. The total mass constraint introduced below is such a particular example. Though we do not consider any further generalizations in the present paper, we should also emphasize that the function F_l for the defining a constraint can take any form, even a one not at all related to a moment in a remote sense, as further discussed in section 6d.

The second implication stems from the maximum entropy principle (Jaynes 2003): it is desirable to constrain a distribution in a physically meaningful manner, rather than just considering it as a simple curve fitting problem. In other words, the choice of the constraint function F_l should better be based on physical considerations, but mathematically in a more general manner, rather than a purely statistical consideration that may lead to a choice of a type of moments. A specific choice of the constraints below is also based on this consideration.

From a point of view of observational measurements, we may further insist that a distribution is best constrained by an available set of measurements. Use of the CVI mass measurement is a particular example considered here. It further leads to a perspective that in order to estimate a PSD, no information on the PSD itself may be necessary, but only the observational information on the bulk integrated constraints C_l ($l = 1, \ldots, N$) is required, as long as the assumed PSD Eq. (4.2) is well physically based so that a certain universality can be expected.

As specific constraints we take the mean size $\overline{D}$ and the total mass M of the particles per volume; that is,

$$C_1 = \int_{D_{\min_1}}^{D_{\max_1}} p(D)\,D\,dD\,, \tag{4.5a}$$

$$C_2 = \int_{D_{\min_2}}^{D_{\max_2}} p(D)\,m(D)\,dD\,, \tag{4.5b}$$

and $C_1 = \overline{D}$, $N_T C_2 = M$, where N_T is the total particle number density, and $m(D)$ is the particle mass defined as a function of the size D. Furthermore, the distribution density $p(D)$ is introduced by $p = N/N_T$.

Here, the total particle concentration N_T is estimated from the particle probe measurements based on the formula

$$N_T = \int_{D_{\min}}^{D_{\max}} N(D)\,dD\,. \tag{4.6}$$

As a result, the distribution density $p(D)$ is normalized as

$$\int_{D_{\min}}^{D_{\max}} p(D)\,dD = 1.$$

As a rule, the integral range $[D_{\min,l}, D_{\max,l}]$ (l = 1, 2) in Eqs. (4.5a) and (4.5b) is the same as the range, $[D_{\min}, D_{\max}]$, considered for the particle probe data. As discussed in section 2, three ranges are considered: full, medium, and narrow. An exception to this rule is when the CVI measurement is used for estimating the constant C_2. In the latter case, the range $[D_{\min_2}, D_{\max_2}]$ is set to the range of the validity of the CVI measurements, 7 μm–2 mm, as discussed in section 2.

To perform the integral (4.5b), the particle mass $m(D)$ must also be specified as a function of the size D. In practice, the mass–size relationship differs from one particle habit to another, and estimating the optimized relationship for a given dataset is an important subject in its own right. In the present study, however, we simply follow the Eq. (2.1) introduced by Heymsfield et al. (2002), as discussed in section 2, but with different coefficient values introduced earlier. In the next section, we will consider two cases: the first fully considers the two constraints (4.5a) and (4.5b), and the second only the single constraint (4.5b). The assumed PDF forms for each case are discussed in the reminder of this section.

a. *Under two constraints*

As for distributions under the two constraints, we consider two additional possibilities:

$$p(D) = n_0 \exp(-\lambda_1 D - \lambda_2 D^b) \quad \text{and} \tag{4.7a}$$

$$p(D) = n_0 D^{b-1} \exp(-\lambda_1 D - \lambda_2 D^b) \tag{4.7b}$$

along with the gamma distribution introduced by Eq. (3.1). These additional distributions are obtained by applying the general result from the maximum entropy principle [Eq. (4.3)] with the mean size and particle mass [Eqs. (4.5a) and (4.5b)] as the constraints and by taking the particle size D and mass m, respectively, as a restriction variable (Yano et al. 2016). Thus, the contrast of the results between the gamma distributions and these two serve as a further test of applicability of the maximum entropy principle to PSDs.

b. *Under a single constraint*

An ultimate goal of this study is to seek the possibility of estimating a PSD based only on bulk characteristics of the hydrometeors, which are measured by other instruments independent of the particle probes. The IWC measured by CVI is an example. The mean size $\overline{D}$ on the other hand, does not fall into the category of bulk characteristics, because the value is obtained only by averaging over all the particle measurements for a given flight leg segment.

Thus, the possibility of constraining a distribution only by mean content [Eq. (4.5b)] is to be considered. For considering this possibility, we further simplify the distributions by setting $\mu = 0$ in Eq. (3.1) and $\lambda_1 = 0$ in Eqs. (4.7a) and (4.7b):

$$p(D) = n_0 e^{-\lambda D}, \tag{4.8a}$$

$$p(D) = n_0 \exp(-\lambda_2 D^b), \quad \text{and} \tag{4.8b}$$

$$p(D) = n_0 D^{b-1} \exp(-\lambda_2 D^b). \tag{4.8c}$$

The last two distributions are obtained under a single constraint with the mean mass [Eq. (4.5b)].

5. Analysis

In presenting the results in this section, we show the number density $N(D)$ rather than the distribution density $p(D)$ in order to enable a direct comparison of the results with those from the standard method described in the last section. The former is obtained from the latter simply by multiplying the total particle number density N_T: $N(D) = N_T p(D)$.

We measure the PSD-fit error under a double-logarithmic scale by

$$\text{err} = \left\{ \frac{\displaystyle\int_{D_{\min,0}}^{D_{\max,0}} \frac{1}{D} [\log_{10} N(D) - \log_{10} N_{\text{obs}}(D)]^2\, dD}{\log_{10} D_{\max,0} - \log_{10} D_{\min,0}} \right\}^{1/2}. \tag{5.1}$$

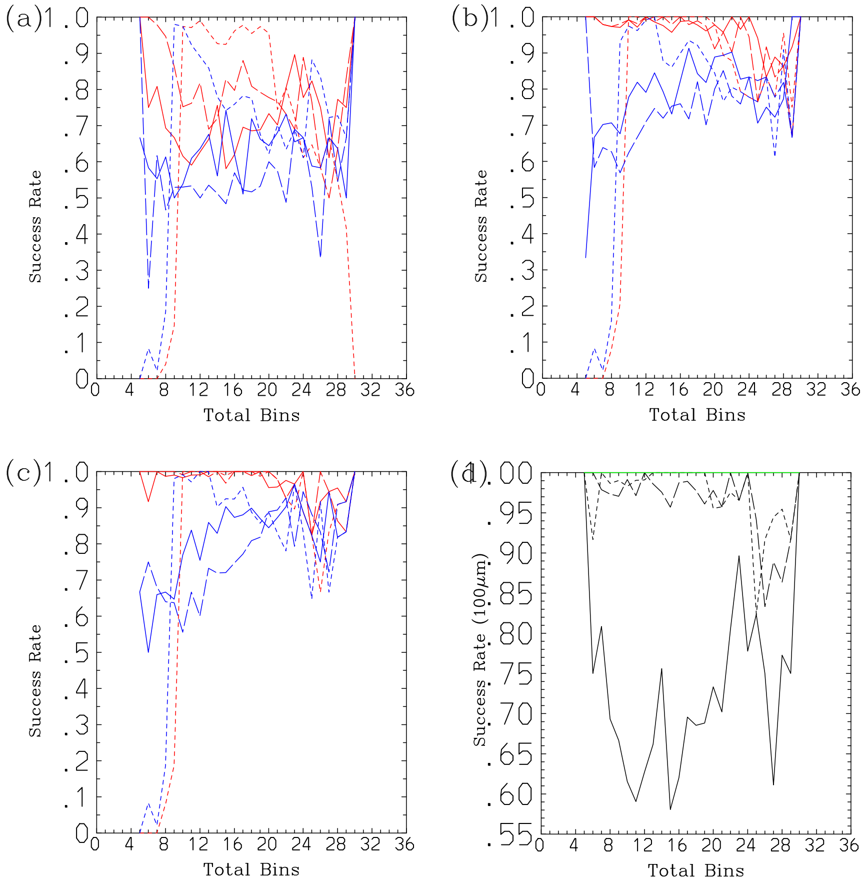

FIG. 3. The mean success rate of the minimization of Eq. (4.4) as a function of the total bins assuming the PSD forms (a) $N_0 D^{\mu} \exp(-\lambda D)$ [Eq. (3.1)], (b) $n_0 \exp(-\lambda_1 D - \lambda_2 D^b)$ [Eq. (4.7a)], and (c) $n_0 D^{b-1} \exp(-\lambda_1 D - \lambda_2 D^b)$ [Eq. (4.7b)]. The curves are for the full (solid), the medium (150 μm–10 mm: long dashed), and the narrow ranges (0.55 μm–5 mm: short dashed). The cases with the total mass density (IWC) M based on particle probes in red, and those based on CVI in blue. (d) Summary for (a)–(c): fits to the PSD forms [Eq. (3.1): solid], [Eq. (4.7a): long dashed], and [Eq. (4.7b): short dashed] for the full range (100 μm–18 mm) with IWC also measured by the particle probes. The green curve is under the traditional method.

Here, the integral range, $[D_{\min,0}, D_{\max,0}]$, is taken to the full available size range, 100 μm–18 mm, regardless of the range adopted for fitting PSD. The integrals are approximated by a sum of the values at each size bin multiplied by a bin size, as presented by, for example, Eq. (1) in Heymsfield et al. (2013), and a bin for a missing observation is simply omitted from the sum.

Note that the error measure (5.1) is designed to directly quantify the degree of the fit under the double-logarithmic plot (as shown by Figs. 6, 7, 11, and 12 below). As pointed out by McFarquhar and Heymsfield (1997), different error measures provide qualitatively different results. Recall that we minimize Eq.(4.4) for obtaining the PSD $N(D)$. Equation (5.1) is used merely for evaluating the errors of the obtained PSD.

a. *Under the two constraints*

Here, the PSD forms are optimized under the two constraints: the mean size $\overline{D}$ and the IWC M. The minimization procedure introduced in the last section does not always work, possibly partially because of a specific numerical procedure, especially owing to the initialization of the iterations (see appendix). The success rate of the procedure is shown in Fig. 3 as a function of the total measured bin number. In all three cases, the success rate tends to cluster around the choices of a mass measurement method: estimates based on particle probes tend to present higher success rates than those based on the CVI. The success rates for the former is most of the time above 70%, whereas for the latter is often less than 60%, and even remains close to 50% with the gamma distribution fit (Fig. 3a). An exception to this rule is when the

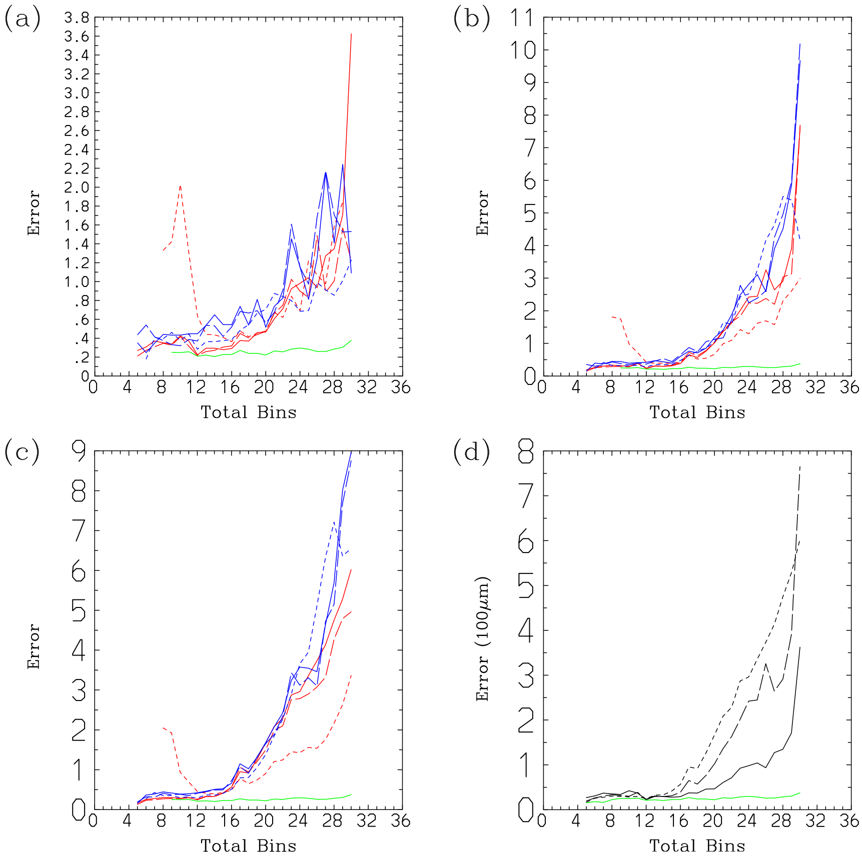

FIG. 4. As in Fig. 3, but for the fitting errors. Furthermore, the errors under the traditional method are added as a green curve in all the frames.

narrow size is used with the CVI (blue short dashed): the success rate becomes comparable to the cases with the particle probe–based mass. This is possibly coincidental, owing to a tendency that the largest particles only partially enter the CVI inlet. Another noticeable feature is that the narrow range cases (short dash) both with the particle probe– (red) and CVI-based IWC (blue) perform relatively well, but only when the total bin number is above 8.

Figure 3d summarizes the performance of the fit to these three PSD forms by choosing the case with the full range with the IWC based on the particle probes. The success rate for the traditional approach is also included with a green curve: it is almost perfect for the total bin numbers above 5. The fits to the PSD forms [Eqs. (4.7a) and (4.7b)] defined under the maximum entropy principle succeed more than 95% of times for the range of the total bin numbers 2–22. The fit to the gamma distribution only has a success rate about 70%.

The fitting error (5.1) under the traditional method is shown by the green curve in all the frames of Fig. 4 as a reference: the mean error is always less than 0.5 for all the total bin numbers under the traditional method. There is a great deal of contrast with the errors associated with estimates based on the proposed new method as shown in Figs. 4a–c by the other curves. In all cases, the error increases rather dramatically above about 16 total bins, with the increasing bin numbers. We will further discuss the implications in section 6c.

As for the success rates (Fig. 3), the errors are clustered by the choice of the mass measurement methods: IWC based on the particle probe systematically provides (red curves) better fit than those based on CVI (blue curves). This is rather expected, because CVI-based IWC is not consistent with the PSD data provided by the particle probes. Nevertheless, the relative success with the CVI-based fit may be considered encouraging. We also note that the change of the fitting range does not represent any consistent tendency for deteriorating the fitting error, although the fitting error itself is defined for the whole size range.

A summary of these results is given in Fig. 4d: the traditional fitting method (green curve) always performs well independent of the total bin number. Below total bin number 12, the proposed new method also works equally well, but above the total bin numbers 12, 16, and

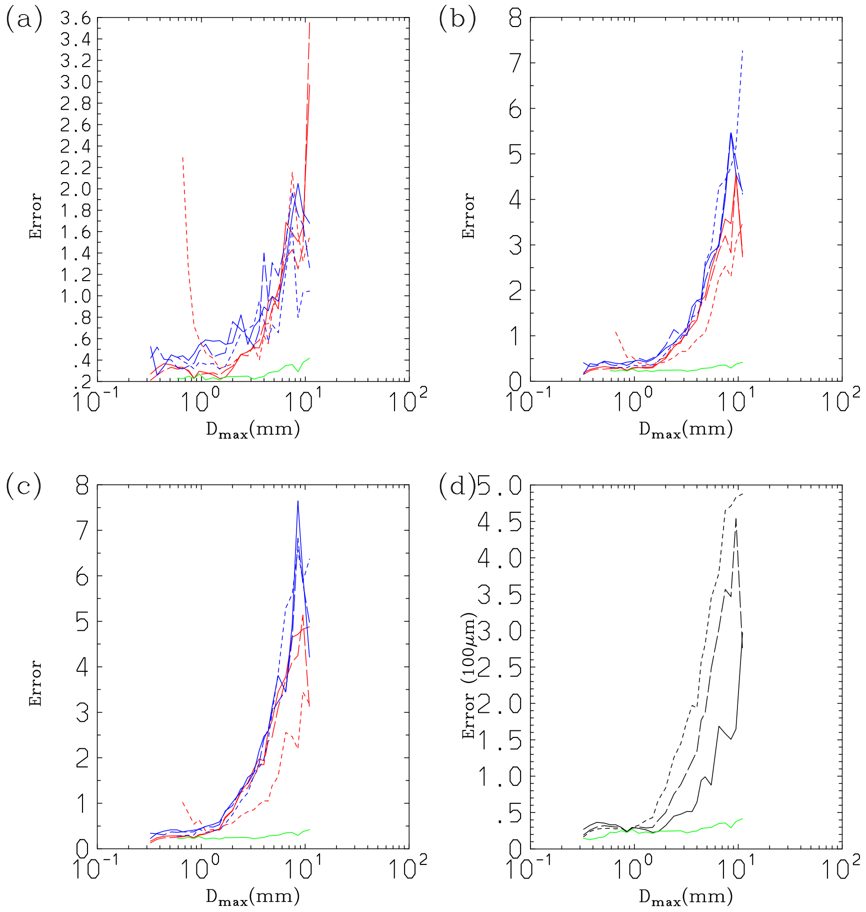

FIG. 5. As in Fig. 4, but as functions of the maximum size.

20, respectively, the error suddenly increases for the forms (4.7b), (4.7a), and (3.1). The gamma distribution also fits the best to data even under the new method.

Figure 5 is as in Fig. 4, but for functions of the maximum size. Though the correspondence is not one to one, we see qualitatively the same results, because the mean maximum size generally increases with increasing available bin numbers. In particular, the error suddenly begins to increase above the 2-mm maximum size with the new fitting method.

Finally, two examples of the actual curve fit results when the full range is used are shown with the particle probes and CVI for IWC, respectively, in Figs. 6 and 7. Here, we have chosen particular cases that the four curve fits diverge well enough so that we can see differences. In many cases, those four curves fit together rather well, as the statistics in Figs. 4 and 5 above suggest.

The first example (Figs. 6a and 7a) is with a relatively narrow size range with a maximum size of 2 mm. This is a case where the traditional gamma fit (double-chain dashed) substantially underestimates (overestimates) the PSD in the small (large) size limit compared to the observation (solid). In this case, the new method provides a much better fit overall, with the exception of the gamma distribution fit with the IWC constrained by CVI (long dashed in Fig. 7a). The second (Figs. 6b and 7b) is a typical example when a large number of bin measurements is available: the gamma distribution can fit to the data (solid curve) well based on traditional (double chain) method. The fit based on the new method works less well for all the three distributions forms considered. The performance with the all three forms is also fairly comparable when the IWC is constrained by CVI (Fig. 7b). On the other hand, the gamma distribution fit performs clearly the best, and the distribution with Eq. (4.7a) the second, when the IWC is constrained by the particle probes (Fig. 6b).

b. *Under a single constraint*

Here, the distribution forms (4.8a), (4.8b), and (4.8c) are optimized solely based on the constraint of the total mass (IWC) M after a normalization in terms of the total particle concentration N_T. Arguably, an estimation of the mean size $\overline{D}$ is statistically explicitly dependent on an

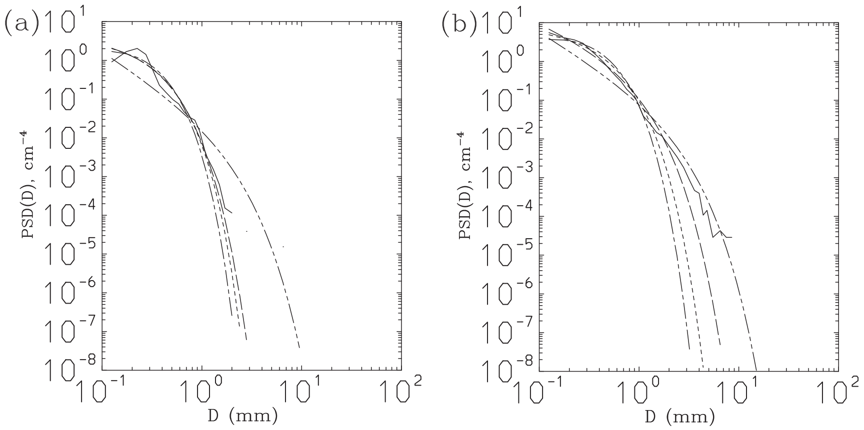

FIG. 6. Two examples of fit of PSD measurements (solid) into prescribed forms: $N_0 D^{\mu} \exp(-\lambda D)$ [Eq. (3.1): long dashed], $n_0 \exp(-\lambda_1 D - \lambda_2 D^b)$ [Eq. (4.7a): short dashed], and $n_0 D^{b-1} \exp(-\lambda_1 D - \lambda_2 D^b)$ [Eq. (4.7b): chain dashed] based on the minimization method, and the gamma distribution under the traditional method (double-chain dashed): (a) a case with 8 bin measurements and (b) a case with 30 bin measurements. Here, IWC is constrained by the particle probe measurements.

observed PSD. Thus, the idea to be tested here is to estimate the performance of the new methodology by excluding the more explicitly PSD-dependent information.

Figures 8–10, respectively, show the corresponding results as for Figs. 3–5. A reduction of a number of parameters clearly facilitates a procedure for identifying the minimum, and as a result, the success rate overall increases: all the cases have almost 100% success rate above the total bin number 8 and $D_{\max} = 0.1$ mm. In spite of the decrease of the number of free parameters, the deterioration of the fit to the observations is not dramatic: the deterioration is the least with the gamma distribution (Figs. 9a and 10a), but the deterioration becomes gradually more apparent to the order of the fits to Eqs. (4.8b) and (4.8c).

Examples of a fit are shown in Figs. 11 and 12: the same cases as for Figs. 6 and 7 are shown. Comparison of the two pairs suggests that a reduction of fit performance due to a reduction of the number of the parameters is relatively small as suggested above.

6. Discussion and conclusions

a. Proposed basic principle

The present study has proposed the determination of the PSD as a physical problem rather than as a mere curve-fitting procedure. The study has been inspired by the maximum entropy principle (Yano et al. 2016), which can define the most likely distribution of a

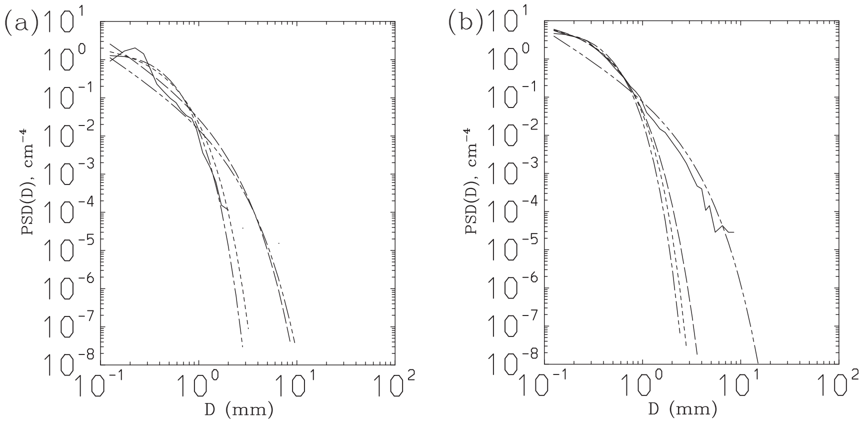

FIG. 7. As in Fig. 6, but using the CVI-based IWC.

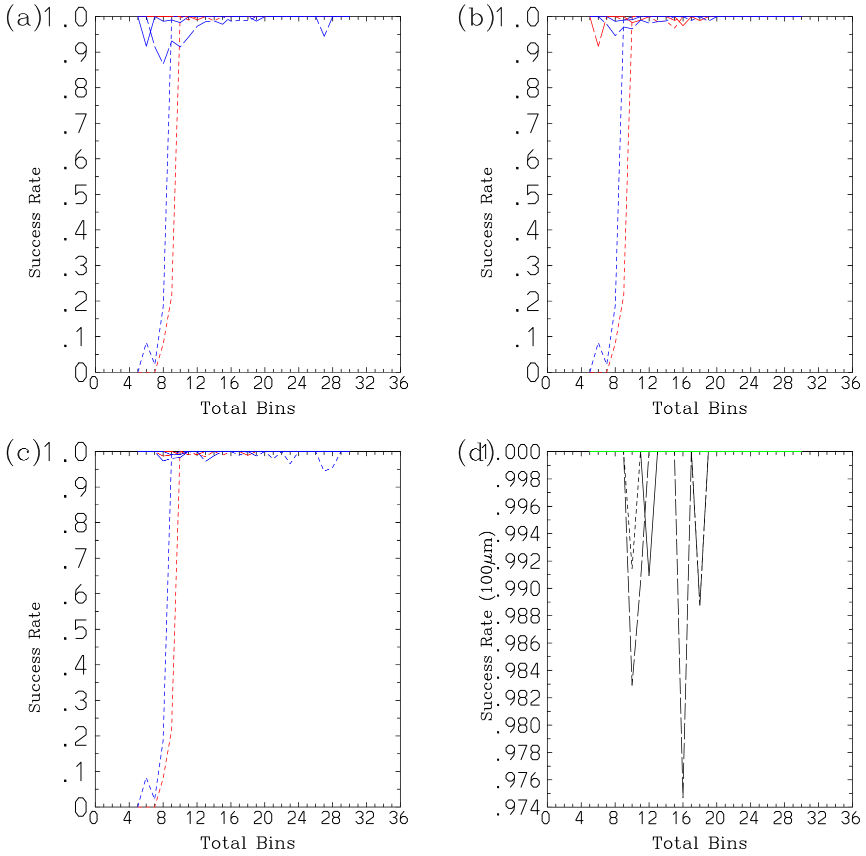

FIG. 8. As in Fig. 3, but for the cases under a single constraint.

variable when a set of physical integral constraints are known. The constants (parameters) of the derived distribution are determined from an imposed set of integral constraints. The main starting point of the present study has been to realize that this last procedure can be used in its standalone manner. A general distribution form must be prescribed in a certain manner but not necessarily based on the maximum entropy principle. The present study provides a proof of this concept by analyzing the ice particle measurements from the TC4 campaign (Toon et al. 2010).

The conventional wisdom would be that in order to determine the hydrometeor particle size distribution (PSD) observationally, the particle sizes must be directly measured, say, with optical probes. Unfortunately, collecting in situ particle size distribution data is expensive. In this respect, the proposed methodology is potentially powerful, because it suggests estimating the PSD solely based on the integrated physical characterizations of the hydrometeors instead of counting every hydrometeor. As a result, the task of the particle probes reduces to that of carefully counting the total particle concentration.

Integrated constraint can be alternatively provided, for example, by the total mass measured by the counterflow virtual impactor (CVI). To see this possibility explicitly, the CVI data are also used in the present study as an alternative source for the total mass constraint. The overall fit error increases with use of the CVI data, owing to the discrepancy between the CVI and particle probe data for the IWC, but only by a relatively minor degree. Arguably, this method may even self-correct the PSD form by providing a more reliable IWC measurement.

We may further argue that bulk quantities such as mean size and total mass are likely to provide more reliable information than the individual counting of hydrometeors. The new methodology proposes to exploit this bulk information more fully. This general approach also permits us to focus on a narrower range of the particle sizes where the measurements are more reliable. If the prescribed general form is ever "physically based," a proper fitting procedure would allow us to extrapolate the result.

The bulk information that can be adopted under this methodology is completely general so long as they are expressed in terms of a general integral form (4.1), an integral of the PSD weighted by a certain function.

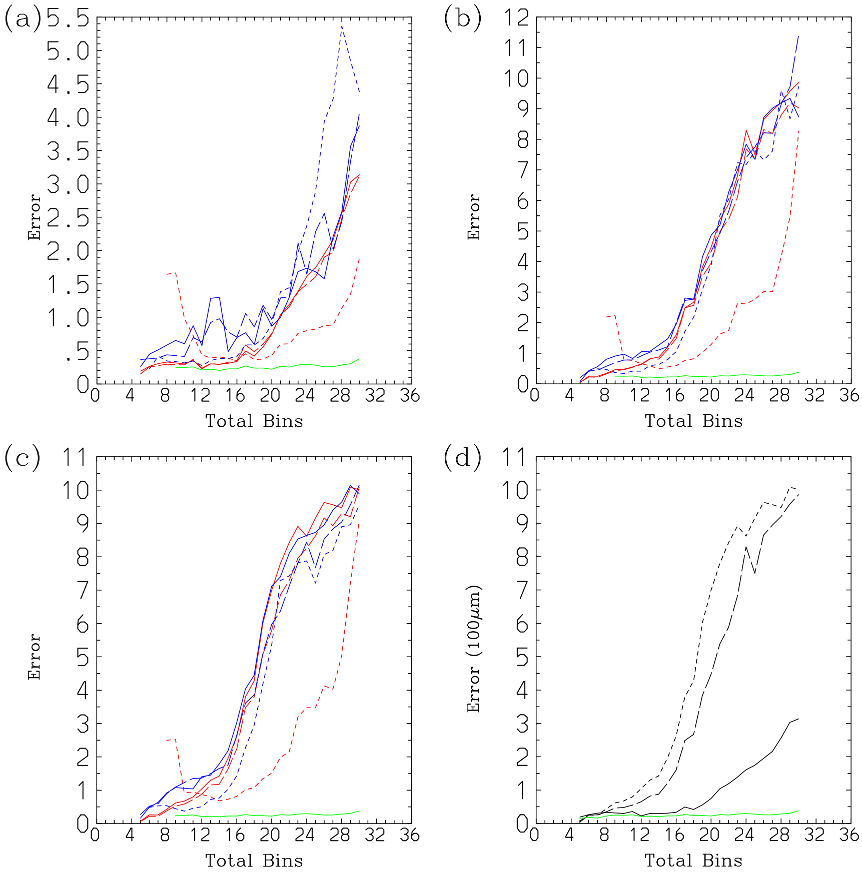

FIG. 9. As in Fig. 4, but for the cases under a single constraint.

b. Test study

In this study, the total particle concentration, total mass (IWC), and the mean particle size are adopted as the integrated physical constraints of the problem. The gamma distribution and the two distributions obtained under the maximum entropy principle by taking the size and the particle mass, respectively, as a restriction variable are adopted as distribution functions to fit. The fitting errors [Eq. (5.1)] of the PSD for these prescribed distributions with the proposed method [Eq. (4.4)] are comparable to those based on the measurements, especially when the observed maximum particle size is less than 2 mm. The same method is further applied to the case when distributions are constrained only by the total particle number concentration and the mass (IWC). In spite of a further decrease of free parameters for the distribution form, it is found that the proposed method still works relatively well.

Among the three possible distribution forms adopted for fit, the gamma distribution consistently leads to better results than the other two distributions derived under the maximum entropy principle. Though a physical reason for a superior fit of the gamma distribution is yet unclear, the result suggests an inherent limitation of the maximum entropy principle for estimating the hydrometeor PSDs.

An obvious issue left out of the present study is that of evaluating both the data and the estimation reliabilities as well as associated errors in a more objective manner. In general, when narrowing down the analysis range for the size of hydrometeors, data reliability increases, but the uncertainties associated with the estimation of the PSD form also increases. The optimal analysis range should be ultimately decided based on a compromise between these two opposite tendencies.

c. The tail issue

The test with the new proposed methodology has encountered an inherent difficulty of obtaining a good fit to the tail part of the PSD.

The highest moment that we could identify under this principle was the total particle mass, which only roughly corresponds to the second moment, or the third moment when the particles are spherical. As a

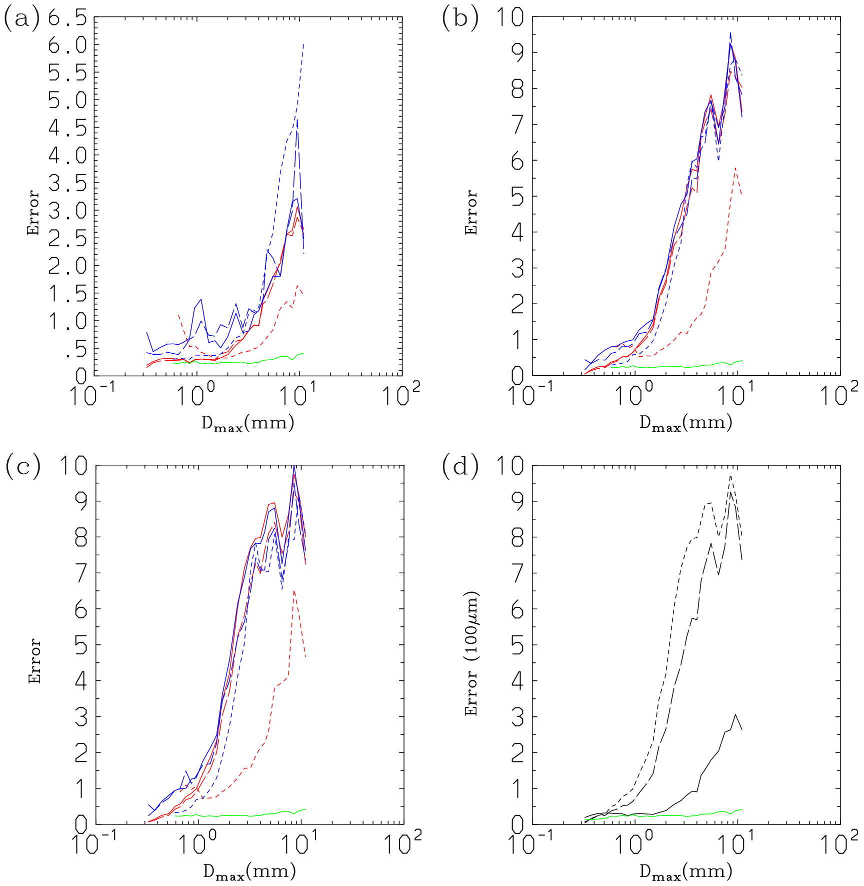

FIG. 10. As in Fig. 9, but as functions of the maximum size.

result, the proposed fitting method faces an inherent difficulty in accurately fitting the PSD to data in the tail part compared to the traditional method, in which the PSD is constrained by the sixth moment. As a result, the fitting error inevitably increases as a measured size range increases, and rather dramatically when the observed maximum particle size exceeds 2 mm. This difficulty may be overcome if we adopt radar reflectivity as an additional physical constraint, for example. Possibilities of exploiting different types of measurements should be further pursued.

On the other hand, as the most basic premise of the present study, if an assumed PSD form is physically based in robust manner, a given set of integral constraints must be sufficient for estimating the PSD accurately, to the extent that the observed integral constraints are accurate enough. From this perspective, an alternative possibility is that the introduced PSD forms from the maximum entropy principle do not describe the tail part of the observed PSD well, and that is the real reason why we have inherent difficulties for an accurate fit in the tail part. One specific possibility is that the tail part distribution is strongly controlled by transient sedimenting ice particles, which are not properly described in the maximum entropy principle due to its transient tendency. This alternative possibility would worth further investigations.

d. *Further perspectives*

The idea proposed here may appear to be not fundamentally original in a practical sense: the traditional methodology (e.g., Kozu and Nakamura 1991; Heymsfield et al. 2002; Zhang et al. 2003; Schmitt and Heymsfield 2009) also fits the observed PSD into the gamma distribution solely based on certain integral constraints called moments. However, the original rationale for using moments for fitting the PSD is that the former well quantifies the latter from a statistical point of view.

On the other hand, the present study considers these constraints from the physical basis and also emphasizes an importance of directly adopting the quantities that can be measured, preferably separately from the particle

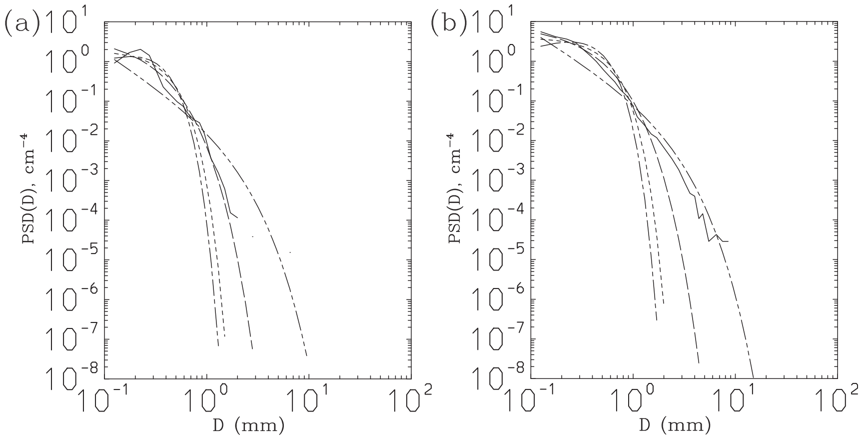

FIG. 11. Examples of fit of SPD measurements (solid) into prescribed forms: $n_0\, e^{-\lambda D}$ [Eq. (4.8a): long dashed], $n_0 \exp(-\lambda_2 D^b)$ [Eq. (4.8b): short dashed], and $n_0 D^{b-1} \exp(-\lambda_2 D^b)$ [Eq. (4.8c): chain dashed] based on the new minimization method, and the gamma distribution under the traditional method (double-chain dashed): PSD measurement as in Figs. 6 and 7. Here, IWC is constrained by the particle probe measurements.

probe measurements. The IWC obtained from the CVI, as considered in the present study, is a particular example. In addition to the in situ cloud measurements, potentially, remote sensing measurements such as those from radar as well as satellite can be adopted as physical constraints. These possibilities should be pursued further.

There are already many attempts for estimating the PSD from the radar measurements (e.g., Seliga and Bringi 1976; Gorgucci et al. 2002; Yoshikawa et al. 2014), but from very different perspectives. The proposed new methodology, on the other hand, establishes a clear link of these attempts to the standard PSD estimate based on the moments, by generalizing the latter. Characteristics obtained from radar measurements, for example, as defined by Eqs. (4)–(6) in Yoshikawa et al. (2014), are considered particular examples of those general physical constraints. Unlike the earlier radar-based PSD retrievals, under this new approach, the only preliminary requirement for the radar data processing is to remove the attenuation effect of the radar signal. Nonattenuated radar parameters can directly constrain the PSD form under the new methodology proposed. This is a particular possibility that is worthwhile to further pursue.

An important ingredient for the success of this approach is that the adopted general PSD form must be physically based to a good extent so that its universality can be anticipated. The present study has not considered the issue of the ‘‘physically based’’ distribution in depth but merely adopted distributions obtained by straight applications of the maximum entropy

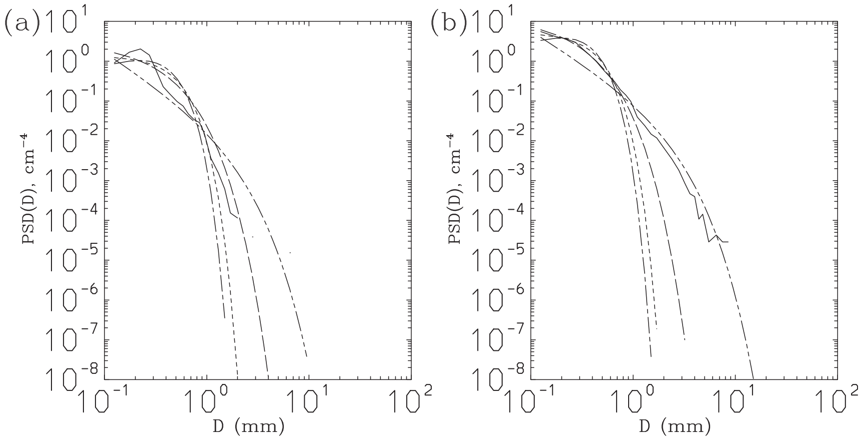

FIG. 12. As in Fig. 11, but using the CVI-based IWC.

principle. As it turns out, those distributions somehow never overperform the standard gamma distribution. The reason for this tendency as well as applicability and the limitations of the maximum entropy principle are issues that warrant further investigation. These investigations are especially important for establishing a robust physical theory for the PSD so that the observed PSDs are interpreted under a more solid physical basis and more readily applied for improving the microphysical modeling.

APPENDIX

Numerical Procedure for the Minimization

The problem at stake is to minimize an integral ϵ defined by Eq. (4.4) against the three parameters in the distributions: Eqs. (3.1), (4.7a), and (4.7b). Here, the first parameter n_0 can always be estimated in a straightforward manner under the normalization condition

$$\int_0^{D_{\max}} p(D)\,dD = 1 \tag{A.1}$$

once the other two parameters are known. By invoking principle (A.1), the problem reduces to that of minimizing ϵ in terms of the two parameters: μ and λ for the gamma distribution (3.1) and λ_1 and λ_2 for the two other distributions [Eqs. (4.7a) and (4.7b)]. Here, under the following iteration procedure, every time one of the other parameters is modified, the value of n_0 is adjusted in such a manner that Eq. (A.1) is satisfied.

In this appendix, in presenting the technicalities of the minimization procedure, we designate these parameters as $\mathbf{x} = (x, y)$. Thus, the problem reduces to the minimization of $\epsilon(\mathbf{x})$ against $\mathbf{x}$. Here, we avoid to evaluate a slope (or gradient) of ϵ, because our preliminary test found finite-difference-based evaluations to be numerically unreliable. For this reason, the minimization is performed by seeking a point with the smallest ϵ in a sequential, iterative manner by more directly comparing the values of $\epsilon(\mathbf{x})$ at the three selective points at each step. This iteration is repeated until the range of the three points is narrowed down enough.

The minimization is performed on the plane consisting of (x, y). Visual inspection suggests that the area with the small ϵ is confined to a narrow "valley" on this plane. Thus, it is effective to perform a minimization in one direction, say in x, under a fixed y first, and then to seek a minimum by changing y.

Thus, the basic sequence of the procedure is as follows:

1) As the initialization, choose the three points $\mathbf{x}_j^*$ ($j = 1, 2, 3$) by setting the edge points for the two parameters as $x_1^* = 0$, $x_2^* = 5$, $y_1^* = 30$, and $y_2^* = 100$ with the gamma distribution and $x_1^* = 0$, $x_2^* = 100$, $y_1^* = 0$, and $y_2^* = 100$ with the two other distributions. We further set $\mathbf{x}_3^* = (\mathbf{x}_1^* + \mathbf{x}_2^*)/2$. These initial conditions are optimized so that the minimization procedure succeeds more often.
2) The minimum points in x direction is sought by an iteration taking $x = x_j^* (j = 1, 2, 3)$ as initial points and fixing y to $y = y_i^*$ with the order of $i = 1, 2, 3$. We set the obtained final minimum as $x = x_c(y)$. Before moving to a new point in y direction, we also reset $x_1^* = x_c/2$, $x_2^* = 3x_c/2$, and $x_3^* = x_c$.
3) In a similar manner, the minimum points in y direction is sought by setting $x = x_c(y)$ and by taking $y = y_j^* (j = 1, 2, 3)$ as initial points. Note that the step 2 constitutes an inner iteration loop of this step: every time we change y, we return to step 2 and seek $x = x_c(y)$.

More precisely, the iteration procedure in x direction is performed in the following manner: After evaluating the error measure ϵ [Eq. (4.4)] for the given three points, we set the points giving the first two minimums for ϵ as x_1 and x_2. Then, we define the three new testing points as $x_1^* = w_1x_1 + w_2x_2$, $x_2^* = (1 + w_2)x_1 - w_2x_2$, and $x_3^* = (x_1^* + x_2^*)/2$ with the weightings defined by $w_i = \epsilon(x_i)/[\epsilon(x_1) + \epsilon(x_2)]$ for $i = 1, 2$.

The iteration in x direction is repeated until one of the following conditions is satisfied:

(i)

$$\left[\left(\frac{x_2 - x_1}{x_m}\right)^2 + \left(\frac{y_2 - y_1}{y_m}\right)^2\right] < \mathrm{err}_c$$

with $\mathrm{err}_c = 10^{-4}$ and

$$\mathbf{x}_m = \frac{1}{2}(\mathbf{x}_1 + \mathbf{x}_2);$$

(ii)

$$\left[\left(\frac{x_2 - x_1}{x_m}\right)^2 + \left(\frac{y_2 - y_1}{y_m}\right)^2\right] < 100\mathrm{err}_c$$

and the number i_x of iteration in x direction has exceeded 100; or

(iii) the number i_x of iteration in x direction has exceeded 1000.

A similar set of conditions is also introduced in y direction for terminating the whole iteration procedure, but in a slightly different manner:

(i)

$$\left[\left(\frac{x_2 - x_1}{x_m}\right)^2 + \left(\frac{y_2 - y_1}{y_m}\right)^2\right] < \mathrm{err}_{c,2}$$

with $\mathrm{err}_{c,2} = 10^{-6}$;

(ii)

$$\left[\left(\frac{x_2 - x_1}{x_m}\right)^2 + \left(\frac{y_2 - y_1}{y_m}\right)^2\right] < \mathrm{err}_{c}$$

and

$$\epsilon[x_c(y_1), y_1] < \mathrm{err}_c;$$

(iii)

$$\left[\left(\frac{x_2 - x_1}{x_m}\right)^2 + \left(\frac{y_2 - y_1}{y_m}\right)^2\right] < \mathrm{err}_{c,3}$$

with $\mathrm{err}_{c,3} = 10^{-3}$ and the number i_y of the iterations in y direction has exceeded 100; or

(iv)

$$\left[\left(\frac{x_2 - x_1}{x_m}\right)^2 + \left(\frac{y_2 - y_1}{y_m}\right)^2\right] < 10\mathrm{err}_{c,3}$$

with $\mathrm{err}_{c,3} = 10^{-3}$ and the number i_y of the iterations in y direction has exceeded 1000.

The last case is considered an abnormal convergence and returned with a flag "failure." Finally, the maximum number of total iterations (i.e., accumulated number of iterations in x direction) is set to 10^5, and the iteration is terminated at that point returning a flag failure.

For a certain value of y, no minimum in the x direction may be found. In this case, the testing points in y must be reset. Assuming $y_1^* < y_2^*$, when $y = y_2^*$ does not find the minimum in x, and $y_1^* > 0$, we reset $y_2^* = 0.2y_1^*$, and if not, $y_2^* = 0.2y_2^*$.

The minimization is also performed in the analogous manner with the case with the distributions (4.8a)–(4.8c). In this case, in order to ensure finding the real minimum, the two points with the smallest values are chosen from the 100 points obtained by dividing the range $[1, 10^3]$ for λ by equal interval. These two points are used as x_1^* and x_2^* for initiating the minimization iteration described above.

Note that the current version of the minimization code is not optimized.

REFERENCES

Baker, B., and R. P. Lawson, 2006: Improvement in determination of ice water content from two-dimensional particle imaginary. Part I: Image-to-mass relationship. *J. Appl. Meteor. Climatol.*, **45**, 1282–1290, https://doi.org/10.1175/JAM2398.1.

Brown, P. R. A., and P. N. Francis, 1995: Improved measurements of the ice content of cirrus using a total-water probe. *J. Appl. Meteor. Climatol.*, **12**, 410–414, https://doi.org/10.1175/1520-0426(1995)012<0410:IMOTIW>2.0.CO;2.

Durrett, R., 2010: *Probability: Theory and Examples*. Cambridge University Press, 380 pp.

Gorgucci, E., V. Chandrasekar, V. R. Bringi, and G. Scarchilli, 2002: Estimation of raindrop size distribution parameters from polarimetric radar measurements. *J. Atmos. Sci.*, **59**, 2373–2384, https://doi.org/10.1175/1520-0469(2002)059<2373:EORSDP>2.0.CO;2.

Hallett, J., 2003: Measurement in the atmosphere. *Handbook of Weather, Climate, and Water: Dynamics, Climate, Physical Meteorology, Weather Systems, and Measurements*, T. D. Potter and B. R. Colman, Eds., Wiley-Interscience, 711–720.

Handwerker, J., and W. Straub, 2011: Optimal determination of parameters from gamma-type drop size distributions based on moments. *J. Atmos. Oceanic Technol.*, **28**, 513–529, https://doi.org/10.1175/2010JTECHA1474.1.

Heymsfield, A. J., and J. L. Parrish, 1978: A computational technique for increasing the effective sampling volume of the PMS two-dimensional particle size spectrometer. *J. Appl. Meteor.*, **17**, 1566–1572, https://doi.org/10.1175/1520-0450(1978)017<1566:ACTFIT>2.0.CO;2.

——, A. Bansemer, P. R. Field, S. L. Durden, J. L. Stith, J. E. Dye, W. Hall, and C. A. Grainger, 2002: Observations and parameterizations of particle size distributions in deep tropical cirrus and stratiform precipitating clouds: Results from in situ observations in TRMM field campaigns. *J. Atmos. Sci.*, **59**, 3457–3491, https://doi.org/10.1175/1520-0469(2002)059<3457:OAPOPS>2.0.CO;2.

——, ——, C. Schmitt, C. Twohy, and M. P. Poellot, 2004: Effective ice particle densities derived from aircraft data. *J. Atmos. Sci.*, **61**, 982–1003, https://doi.org/10.1175/1520-0469(2004)061<0982:EIPDDF>2.0.CO;2.

——, ——, G. Heymsfield, and A. O. Fierro, 2009: Microphysics of maritime tropical convective updrafts at temperature from −20° to −60°. *J. Atmos. Sci.*, **66**, 3530–3562, https://doi.org/10.1175/2009JAS3107.1.

——, C. Schmitt, and A. Bansemer, 2013: Ice cloud particle size distributions and pressure-dependent terminal velocities from in situ observations at temperatures from 0° to –86°C. *J. Atmos. Sci.*, **70**, 4123–4154, https://doi.org/10.1175/JAS-D-12-0124.1.

Jaynes, E. T., 2003: *Probability Theory: The Logic of Science*. Cambridge University Press, 753 pp.

Kliche, D. V., P. L. Smith, and R. W. Johnson, 2008: L-moment estimators as applied to gamma drop size distributions. *J. Appl. Meteor. Climatol.*, **47**, 3117–3130, https://doi.org/10.1175/2008JAMC1936.1.

Korolev, A. V., E. F. Emery, J. W. Strapp, S. G. Cober, and G. A. Isaac, 2013: Quantification of the effects of shattering on airborne ice particle measurements. *J. Atmos. Oceanic Technol.*, **30**, 2527–2553, https://doi.org/10.1175/JTECH-D-13-00115.1.

Kozu, T., and K. Nakamura, 1991: Rainfall parameter estimation from dual-radar measurements combining reflectivity profile and path-integrated attenuation. *J. Atmos. Oceanic Technol.*, **8**, 259–270, https://doi.org/10.1175/1520-0426(1991)008<0259:RPEFDR>2.0.CO;2.

Locatelli, J. D., and P. V. Hobbs, 1974: Fall speeds and masses of solid precipitation particles. *J. Geophys. Res.*, **79**, 2185–2197, https://doi.org/10.1029/JC079i015p02185.

Mallet, C., and L. Barthes, 2009: Estimation of gamma raindrop size distribution parameters: Statistical fluctuations and estimation errors. *J. Atmos. Oceanic Technol.*, **26**, 1572–1584, https://doi.org/10.1175/2009JTECHA1199.1.

McFarquhar, G. M., and A. J. Heymsfield, 1997: Parameterization of tropical cirrus ice crystal size distribution and implications for radiative transfer: Results from CEPEX. *J. Atmos. Sci.*, **54**, 2187–2200, https://doi.org/10.1175/1520-0469(1997)054<2187:POTCIC>2.0.CO;2.

——, T.-L. Hsieh, M. Freer, J. Mascio, and B. F. Jewett, 2015: The characterization of ice hydrometeor gamma size distributions as volumes in N_0–λ–μ phase space: Implications for microphysical process modeling. *J. Atmos. Sci.*, **72**, 892–909, https://doi.org/10.1175/JAS-D-14-0011.1.

Mitchell, D. L., R. Zhang, and R. L. Pitter, 1990: Mass-dimensional relationships for ice particles and the influence of rimming on snowfall rates. *J. Appl. Meteor.*, **29**, 153–163, https://doi.org/10.1175/1520-0450(1990)029<0153:MDRFIP>2.0.CO;2.

Noone, K. J., J. A. Ogren, and J. Heintzenberg, 1988: Design and calibration of a counterflow virtual impactor for sampling of atmospheric fog and cloud droplets. *Aerosol Sci. Technol.*, **8**, 235–244, https://doi.org/10.1080/02786828808959186.

Ogren, J. A., J. Heintzenberg, and R. J. Charlson, 1985: In-situ sampling of clouds with a droplet to aerosol converter. *Geophys. Res. Lett.*, **12**, 121–124, https://doi.org/10.1029/GL012i003p00121.

Ottino, J. M., 1989: *The Kinematics of Mixing: Stretching, Chaos, and Transport*. Cambridge Texts in Applied Mathematics, Cambridge University Press, 364 pp.

Schmitt, C. G., and A. J. Heymsfield, 2009: The size distribution and mass-weighted terminal velocity of low-latitude tropopause cirrus crystal populations. *J. Atmos. Sci.*, **66**, 2013–2028, https://doi.org/10.1175/2009JAS3004.1.

Seliga, T. A., and V. N. Bringi, 1976: Potential use of radar differential reflectivity measurements at orthogonal polarizations for measuring precipitation. *J. Appl. Meteor.*, **15**, 69–76, https://doi.org/10.1175/1520-0450(1976)015<0069:PUORDR>2.0.CO;2.

Smith, P. L., and D. V. Kliche, 2005: The bias in moment estimator for parameters of drop size distribution functions: Sampling from exponential distributions. *J. Appl. Meteor.*, **44**, 1195–1205, https://doi.org/10.1175/JAM2258.1.

——, ——, and R. W. Johnson, 2009: The bias and error in moment estimators for parameters of drop size distribution functions sampling from gamma distributions. *J. Appl. Meteor. Climatol.*, **48**, 2118–2126, https://doi.org/10.1175/2009JAMC2114.1.

Toon, O. B., and Coauthors, 2010: Planning, implementation, and first results of the Tropical Composition, Cloud and Climate Coupling Experiment (TC4). *J. Geophys. Res.*, **115**, 200J01, https://doi.org/10.1029/2009JD013073.

Twohy, C. H., A. J. Schanot, and W. A. Cooper, 1997: Measurement of condensed water content in liquid and ice clouds using an airborne counterflow virtual impactor. *J. Atmos. Oceanic Technol.*, **14**, 197–202, https://doi.org/10.1175/1520-0426(1997)014<0197:MOCWCI>2.0.CO;2.

Ulbrich, C. W., 1983: Natural variations in the analytical form of the drop size distribution. *J. Climate Appl. Meteor.*, **22**, 1764–1775, https://doi.org/10.1175/1520-0450(1983)022<1764:NVITAF>2.0.CO;2.

Willis, P. T., 1984: Functional fits to some observed drop size distributions and parameterization of rain. *J. Atmos. Sci.*, **41**, 1648–1661, https://doi.org/10.1175/1520-0469(1984)041<1648:FFTSOD>2.0.CO;2.

Yano, J.-I., A. J. Heymsfield, and V. T. J. Phillips, 2016: Size distributions of hydrometeors: Analysis with the maximum entropy principle. *J. Atmos. Sci.*, **73**, 95–108, https://doi.org/10.1175/JAS-D-15-0097.1.

Yoshikawa, E., V. Chandrasekar, and T. Ushio, 2014: Raindrop size distribution (DSD) retrieval for X-band dual-polarization radar. *J. Atmos. Oceanic Technol.*, **31**, 387–403, https://doi.org/10.1175/JTECH-D-12-00248.1.

Zhang, G., J. Vivekanandan, E. A. Brandes, R. Meneghini, and T. Kozu, 2003: The shape–slope relation in observed gamma raindrop size distributions: Statistical error or useful information? *J. Atmos. Oceanic Technol.*, **20**, 1106–1119, https://doi.org/10.1175/1520-0426(2003)020<1106:TSRIOG>2.0.CO;2.